


# 3D Printing of Covalent Organic Frameworks: A Microfluidic-Based System to Manufacture Binder-Free Macroscopic Monoliths

## Journal Article

### Author(s):

Royuela, Sergio; Sevim, Semih; Hernanz, Guillermo; [Rodríguez San Miguel, David](#) ; Franco, Carlos; Pané, Salvador; Puigmartí-Luis, Josep; Zamora, Félix; Fischer, Peter

### Publication date:

2023-04-25

### Permanent link:

<https://doi.org/10.3929/ethz-b-000649809>

### Rights / license:

[Creative Commons Attribution 4.0 International](#)

### Originally published in:

Advanced Functional Materials 34(17), <https://doi.org/10.1002/adfm.202314634>

### Funding acknowledgement:

101047081/22.00021 - Magnetoelectric 3D printing technology - the revolution of actuatable composites (SBFI)

# 3D Printing of Covalent Organic Frameworks: A Microfluidic-Based System to Manufacture Binder-Free Macroscopic Monoliths

Sergio Royuela, Semih Sevim, Guillermo Hernanz, David Rodríguez-San-Miguel, Peter Fischer, Carlos Franco, Salvador Pané, Josep Puigmartí-Luis,\* and Félix Zamora\*

Covalent organic frameworks (COFs) have witnessed outstanding developments in the past 15 years, particularly in optimizing their pore structures, linkages, and variety of monomers used in their synthesis. Yet, a significant challenge remains unaddressed: the processability of COFs into macroscopic architectures with arbitrary shapes, as they are typically obtained as unprocessable powders. This study presents a novel strategy to address this issue by developing a 3D printable ink comprising a colloidal water suspension of COF nanoparticles. A microfluidic device is engineered that provides precise control over the gelation process of the COF-based ink, allowing for a layer-by-layer fabrication. As a result, the direct production of large-scale binder-free COF architectures from digital designs is achieved at room temperature and atmospheric pressure while eliminating the use of toxic organic solvents.

materials have undergone significant advancements in their chemistry, particularly in addressing challenges related to their stability<sup>[2]</sup> and tuning their chemical properties.<sup>[3]</sup> These advances have opened the door for their potential application in several fields, such as gas storage and separation,<sup>[4]</sup> catalysis,<sup>[5]</sup> environmental remediation,<sup>[6]</sup> or energy storage and conversion.<sup>[7,8]</sup> Yet, a grand challenge that remains unaddressed is the processability of COFs, specifically in achieving macroscopic architectures composed solely of COFs and with arbitrary shapes.<sup>[9]</sup> COFs are primarily obtained as powders that exhibit limited solubility and do not melt. Therefore, conventional processing techniques based on solution processing or melt-extrusion cannot be applied to COFs,

hindering their use in many potential applications. While alternative processing techniques, such as the compression approach, have been used to shape COFs into pellets or membranes,<sup>[10]</sup> the applied pressure compromises their porosity,<sup>[11]</sup> resulting in limited product's performance.

## 1. Introduction

Covalent organic frameworks (COFs) are porous crystalline organic materials that have attracted a wealth of attention from the scientific community. Since their inception in 2005,<sup>[1]</sup> these

S. Royuela, G. Hernanz, D. Rodríguez-San-Miguel, F. Zamora  
Departamento de Química Inorgánica  
Universidad Autónoma de Madrid  
Madrid 28049, Spain  
E-mail: [felix.zamora@uam.es](mailto:felix.zamora@uam.es)

S. Royuela, F. Zamora  
Condensed Matter Physics Center (IFIMAC)  
Universidad Autónoma de Madrid  
Madrid 28049, Spain

S. Sevim, C. Franco, S. Pané  
Department of Mechanical and Process Engineering  
Institute of Robotics and Intelligent Systems  
Multi-Scale Robotics Lab  
ETH Zurich  
Zurich 8092, Switzerland

J. Puigmartí-Luis  
Departament de Ciència dels Materials i Química Física  
Institut de Química Teòrica i Computacional  
University of Barcelona  
Barcelona 08028, Spain  
E-mail: [josep.puigmarti@ub.edu](mailto:josep.puigmarti@ub.edu)

J. Puigmartí-Luis  
Institució Catalana de Recerca i Estudis Avançats (ICREA)  
Pg. Lluís Companys 23, Barcelona 08010, Spain

F. Zamora  
Institute for Advanced Research in Chemical Sciences (IAdChem)  
Universidad Autónoma de Madrid  
Madrid 28049, Spain

P. Fischer  
Institute of Food Nutrition and Health  
Schmelzbergstrasse 9  
ETH Zurich, Zurich 8092, Switzerland

 The ORCID identification number(s) for the author(s) of this article can be found under <https://doi.org/10.1002/adfm.202314634>

© 2023 The Authors. Advanced Functional Materials published by Wiley-VCH GmbH. This is an open access article under the terms of the [Creative Commons Attribution](https://creativecommons.org/licenses/by/4.0/) License, which permits use, distribution and reproduction in any medium, provided the original work is properly cited.

Correction added on 3 January 2024, after first online publication: the order of the authors was changed in this version.

DOI: 10.1002/adfm.202314634

In recent years, additive manufacturing approaches, commonly known as 3D printing, have revolutionized manufacturing, allowing for the creation of arbitrary shapes with unprecedented design flexibility.<sup>[12]</sup> 3D printing has opened up new possibilities by enabling the fabrication of complex structures that were previously challenging to process using traditional methods.<sup>[13]</sup> While 3D printing has primarily focused on polymers, metals, and composites,<sup>[14,15]</sup> there has been a recent interest in porous materials, including MOFs<sup>[16–20]</sup> and COFs.<sup>[21–24]</sup> This is motivated by the increased performance that will be obtained by shaping them in complex arbitrary shapes since significant improvements in key application areas of COFs and MOFs are expected to come from the use of 3D printed materials, such as 3D printed electrodes in battery technology<sup>[25,26]</sup> and reduced back-pressure in separation columns.<sup>[27]</sup> Thus, several research groups have attempted different 3D printing methodologies to produce macroscopic COF structures; however, most successful attempts rely on using another material for structural support, forming composites with variable COF content, but not pure COF pieces. In the first reported approach, Ke et al. developed a method to 3D print COFs by extruding a Pluronic F127 hydrogel containing an amorphous polymer formed by the COF monomers.<sup>[21]</sup> To obtain a shaped porous and crystalline COF, it was necessary to subsequently dry the 3D printed piece, wash it to achieve partial removal of Pluronic F127, anneal it, and activate it by supercritical CO<sub>2</sub> drying (scCO<sub>2</sub>). Later, Banerjee et al. formulated a 3D printable paste comprising COF monomers and graphene oxide (GO).<sup>[23]</sup> Thanks to the presence of GO, the resulting COF-GO monoliths displayed a foam-like morphology with hierarchical porosity. Another recent approach by Zamora, Segura et al. involved dispersing a small amount of nanolayers of a photoactive COF in a photocurable resin, enabling its use in liquid crystal display (LCD)–3D printing instead of direct ink writing (DIW).<sup>[24]</sup> The resulting monoliths preserved the COF's fluorescence and exhibited sensing capabilities for solvent polarity and acidity. Finally, Wang et al. prepared a printable paste by mixing pre-synthesized COF powder with 1-butanol.<sup>[22]</sup> The authors found that the ink was suitable for DIW printing but that the substrate on which it was printed severely affected its ability to dry without cracking.

These advances have shown the feasibility of 3D printing COFs; however, the reported methods still face significant challenges and limitations, including the production of low-crystallinity materials, the need of extensive post-processing steps, or the use of binders or supporting matrices. The use of binders and matrices in COF 3D printing presents significant drawbacks. These additives increase costs, impose limitations on the loading of COF that can be incorporated due to the percolation matrix threshold, and usually are not porous active materials for potential applications, thus reducing the active surface area of the COF structures and their performance efficiency. Therefore, a methodology that enables the 3D printing of pure COF monoliths without using binders should prove a valuable tool for many future applications.

In this study, we present a stable water-based colloid formulation of COF nanoparticles and a methodology for its use as a 3D printable ink. Capitalizing on our previously described synthesis of COF nanoparticles within surfactant micelles in water,<sup>[28]</sup> we have adapted the procedure to transform the colloidal suspen-

sion into a fully 3D printable COF-based ink. To this end, we have developed a microfluidic device that allows precise control over the aggregation of the COF nanoparticles into a gel. By precisely controlling this gelation process at the printer's nozzle and synchronizing it with the movement of a computer numerical control (CNC) machine, we are able to directly 3D print COF-only monoliths with complex shapes based on their computer design.

## 2. Results and Discussion

### 2.1. Preparation of the COF-Based Ink

The preparation of the COF-based ink begins with the BTCA-TAPB-COF aqueous colloid, prepared in a micellar system formed from a mixture of the surfactants hexadecyltrimethylammonium bromide (CTAB) and sodium dodecyl sulfate (SDS) in a 97:3 ratio, which prevents the aggregation of the nanoparticles, as described in **Figure 1a**. As previously reported, the addition of certain solvents such as ethanol causes the precipitation of the nanoparticles. This is due to its ability to solubilize the surfactants, consequently disassembling the micelles and allowing the interaction between COF particles. Thus, they aggregate, and a solid COF is formed. By performing this process inside a microfluidic device that works as the printing nozzle, we hypothesize that we can control the solvent ratios, mixing, and aggregation speed to generate a continuous stream of solid COF without clogging the channel and 3D printing it (**Figure 1b**). However, several modifications were necessary to transform this colloidal suspension into a functional 3D printing ink that, upon flocculation, forms a cohesive pure COF solid (a gel in our case) and not a loose particulate precipitate. These involved adjustments to the synthetic procedure, treatment of the colloid, and flocculation methodology, mainly affecting the ink's concentration and viscosity.

For effective 3D printing, achieving an appropriate concentration of COF nanoparticles in the colloid is crucial so that the COF particles aggregate into a gel after flocculating. In our prior research,<sup>[28]</sup> the colloid's concentration was  $\approx 0.5 \text{ mg mL}^{-1}$  of COF nanoparticles, which proved to be insufficient for 3D printing. At such low concentrations, only a minimal amount of material could be deposited in each layer during the printing process. Subsequently, we increased the concentration of the monomers 1,3,5-triformylbenzene (BTCA) and 1,3,5-tris(4-aminophenyl)benzene (TAPB) to their respective solubility limit in the CTAB/SDS micellar system. The solubility limit for BTCA was found to be  $\approx 2.8 \text{ mg mL}^{-1}$ , while for TAPB was determined to be  $\approx 4.4 \text{ mg mL}^{-1}$ . The resulting colloid contained a concentration of ca.  $3 \text{ mg mL}^{-1}$  of BTCA-TAPB-COF nanoparticles, representing a sixfold increase compared to the previously reported concentration.<sup>[28]</sup> This increase in concentration had a minimal impact on the particle size, with a slight increase from 18 to 20 nm, as determined by dynamic light scattering (DLS) and scanning electron microscopy (SEM) (**Figures S1 and S2**, Supporting Information). However, the concentration change had an effect on the colloid's viscosity, which increased from 1.12 to 2.79 mPa s at 28 °C. Despite the increase in concentration, the colloid did not display the necessary characteristics to function as a suitable printable ink because gelation did not take place after

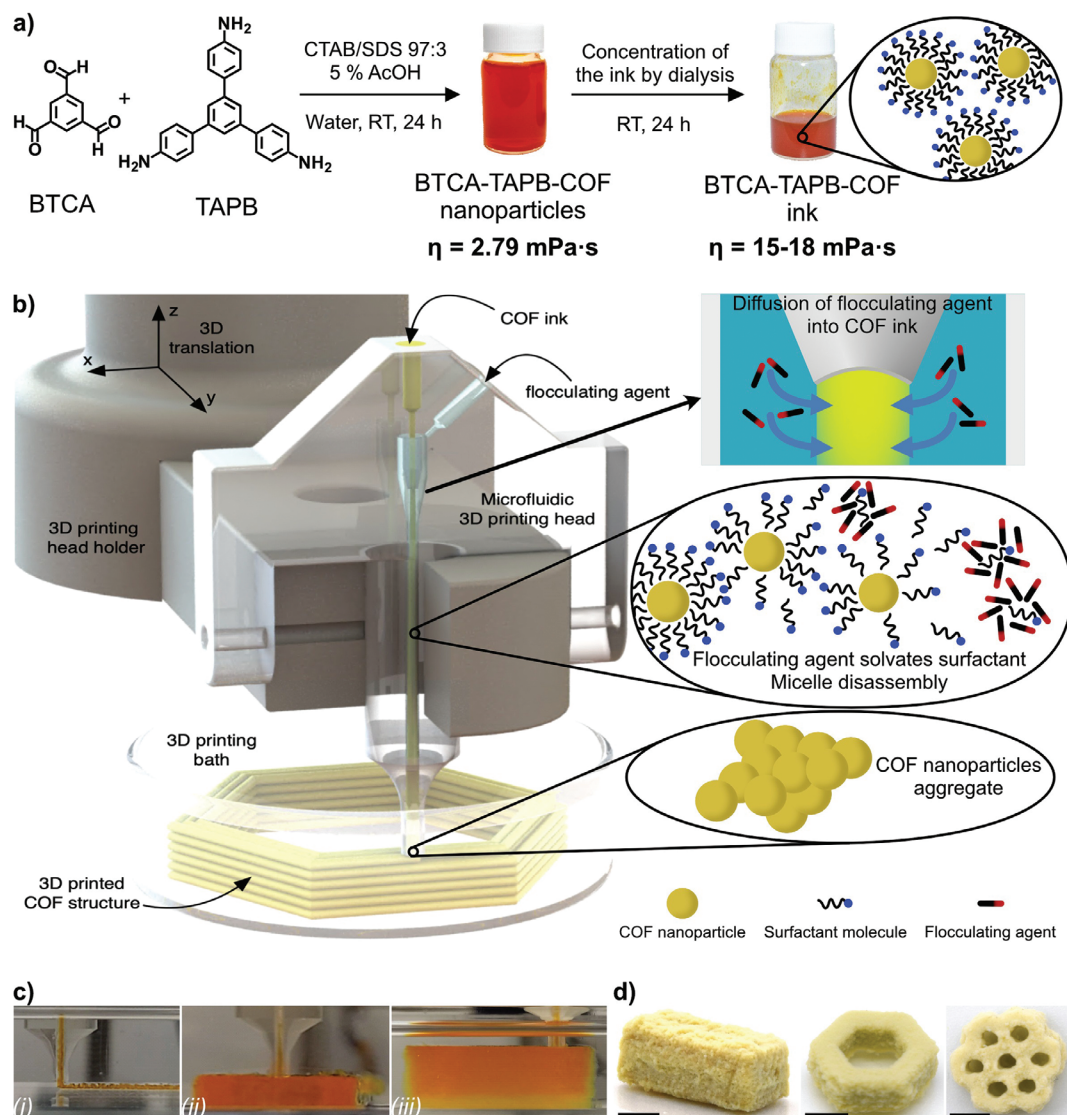


**Figure 1.** a) Schematic representation of the synthesis of BTCA-TAPB-COF colloidal nanoparticles and its dialysis into BTCA-TAPB-COF ink. b) Schematic representation of the microfluidic device that acts as the 3D printing head, integrated into the 3D printer and printing a 3D hollow hexagon COF architecture. The main processes that take place inside the printing head are schematically depicted on the right side. c) Photographs at different times of a BTCA-TAPB-COF monolith being printed. d) Photographs of activated BTCA-TAPB-COF monoliths with a rectangular prism, hollow hexagon, and hexagonal mesh shapes (scale bar: 5 mm).

being mixed with an alcohol. Instead, the COF material formed a loose aggregate.

To increase the COF concentration of the colloid beyond the limits imposed by the maximum solubility of the monomers, the pristine colloids were subject to a process of dialysis. The COF colloid was placed inside a dialysis membrane, while a concentrated aqueous solution of polyethylene glycol (PEG) was placed outside the membrane. The higher osmotic pressure of the PEG solution causes water to be drawn out of the COF colloid, while the COF nanoparticles and PEG molecules remain separated in their original solutions as they are too large to cross the dialysis membrane. Thus, this process results in removing water from the COF colloid, whose volume is reduced by  $\approx 45\%$ , resulting in an increased COF concentration of  $5.4 \text{ mg mL}^{-1}$ . Through-

out this process the nanoparticles' size remained stable at 20 nm (Figures S1 and S2, Supporting Information), the viscosity of the COF-based ink increased to  $\approx 17 \text{ mPa s}$  at  $28^\circ\text{C}$  and, more importantly, upon the addition of an alcohol the COF nanoparticles immediately aggregate into a gel, which allowed us to test its printability.

## 2.2. Development of the 3D Printer

To achieve precise control over the flocculation of the COF-based ink for 3D printing, we engineered a custom-made microfluidic system to be used as the printing head. It consists of two separate streams, one for the COF-based ink and another for the

flocculating agent (e.g., ethanol) that merge into one, leading to the printing nozzle (Figure 1b). Thanks to the design of the device and its reduced dimensions, when the two streams meet laminar flow is maintained, and the mixing of the flocculating agent occurs in a controlled manner via diffusion into the COF stream, gradually solvating the surfactant molecules and allowing the aggregation of the COF nanoparticles into a gel during the residence time in the device. The streams are pushed into the microfluidic system with a pressure-based microfluidic flow controller that allows individual control of the flow rate of each stream.

The printing head, fabricated in our laboratory, features two inlets that merge into the main channel with the outlet located at the tip of the printing head. The geometry in which the channels merge is critical for the proper working of the device, since turbulent mixing or contact of the COF gel with the channel walls leads to non-uniform flows and clogging of the nozzle. Therefore, we opted for a concentric geometry to merge the channels, with the COF channel at the center. Thus, when the two streams meet, the COF-based ink flows along the inner core of the main channel, completely surrounded by the flocculating agent flowing on the outer section of the main channel. As the flow progresses down the channel, the two streams mix gradually by diffusion, leading to the flocculation of the COF nanoparticles and the formation of a COF gel at the tip of the printing head.

To transform this setup into a functional 3D printing system, we integrated it with a CNC machine by replacing the extruder of a commercial Ender 5 fused deposition modeling (FDM) 3D printer with our microfluidic device. The CNC machine's movement is controlled using standard g-code programming language, allowing us to design structures with any computer-aided design (CAD) software, convert them to the corresponding g-code, and 3D print these designs.

### 2.3. 3D Printing Process

We initially attempted to print BTCA-TAPB-COF directly onto glass using a layer-by-layer approach with ethanol as the flocculating agent. However, the printed pieces exhibited poor stability, with weak layer-to-layer adhesion, a tendency to collapse under their own weight after reaching a height of only 5 mm, and were contaminated with significant amounts of surfactants. To address these issues, we decided to perform the printing immersed in a bath of ethanol, which reduced the stress of gravity on the pieces and allowed for efficient dilution of the surfactants. However, the movements of the printing head in the fluid caused turbulence in the bath that damaged the COF pieces, so we changed ethanol for the more viscous 2-butanol, both as the flocculating agent and the printing bath, achieving excellent results (Figure 1c). This allowed us to successfully print well-defined structures with relatively large thicknesses, comprising over 50 layers of BTCA-TAPB-COF, with different geometries such as cubes, cylinders, or hexagons (Figure 1d; Figure S3, Supporting Information). The hydrostatic pressure and higher viscosity of 2-butanol likely contributed to improving the stability during the printing process. Printing within the 2-butanol bath also removes water and surfactants that are present in the COF-based ink, thus leaving structures fully made of COF nanoparticles. These prints can be car-

ried out on different substrates, including glass, polypropylene, polystyrene resin, or silicon dioxide, and directly from their computer design.

As the viscosity of the printing bath seemed to be an important factor in the quality of the printing process, we decided to perform rheological studies of the inks to better understand their behavior inside the printing head. An initial frequency time sweep at a constant deformation and frequency was used to explore the properties of the native COF colloid and revealed constant values for storage modulus, loss modulus, and complex viscosity over time, showcasing the stability of the ink before any external shear application (Figure S4, Supporting Information). Then, to mimic the conditions during the printing process, a constant shear rate of  $50 \text{ s}^{-1}$  was applied, revealing a notable decrease in shear viscosity, which means that the colloid presents a shear-thinning behavior facilitating its flow through the microfluidic channels. Finally, the recovery evaluation after the shear application showed a partial recovery in storage modulus, loss modulus, and complex viscosity, indicative of self-healing properties. Additionally, to understand if the ink turns printable after the dialysis concentration because of the increased viscosity or the high COF nanoparticles concentration, we decided to run a printing test keeping a low COF concentration but increasing the viscosity by adding PEG to the ink. With this ink formulation, the COF failed to form a stable gel (Figure S5, Supporting Information), showing that it is critical to maximize COF concentration in the inks to achieve successful printing and that viscosity plays a secondary role.

Now, we set to optimize the printing conditions, such as the flow rate of the ink (i.e., COF nanoparticle colloid), the flocculating agent (i.e., 2-butanol), the traveling speed and height of the printing head, and the line and layer dimensions. Under optimized conditions, the individual filaments extruded from the printing head are below  $300 \mu\text{m}$  in diameter and when deposited next to each other get fused into a continuous gel phase, resembling the self-healing process observed in many gels.<sup>[29,30]</sup> This leads to monoliths with continuous and homogeneous surfaces, free from cracks or gaps between filaments. This uniform morphology extends throughout the interior of the monoliths and can be observed when they are cut in half (Figure S6, Supporting Information). To show the importance of controlling the in situ aggregation of the COF nanoparticles in the printing head, we show in Figure S7 (Supporting Information) the result of printing with inadequately adjusted parameters such as flow rates, printing speed, layer height, or line width. Self-healing does not occur; instead, the resulting prints exhibit separate and distinct filaments that detach from each other, making the structure mechanically unstable and unsuitable for use. To test the resolution limits of the printing process, we designed a piece with several lines of increasing thickness (Figure S8a, Supporting Information). We found that structures below  $850 \mu\text{m}$  are not mechanically stable and break during the post-processing steps. However, it should be noted that, above that minimum feature size, the resolution of the printer is close to  $250 \mu\text{m}$  (Figure S8b, Supporting Information).

Once the printing is completed, 2-butanol is replaced with ethanol through solvent exchange, and the final structures undergo activation through supercritical  $\text{CO}_2$  drying. This is an improvement over previously reported methods, which require heating the printed prototypes to high temperatures for several

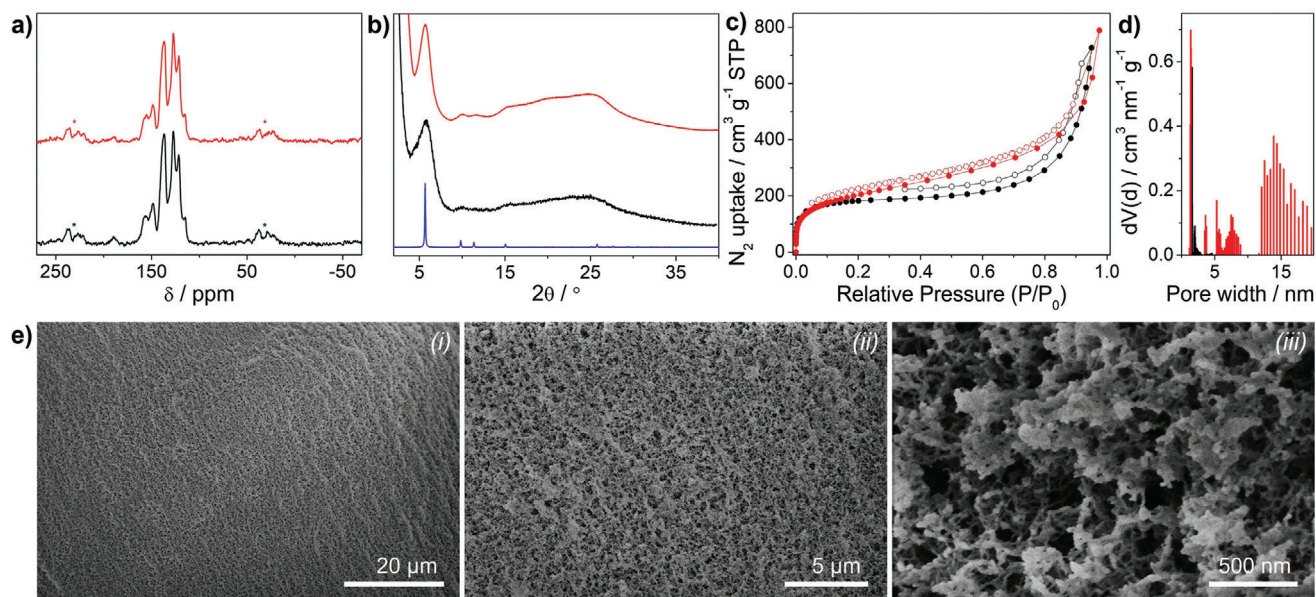


**Figure 2.** a)  $^{13}\text{C}$ -CP/MAS-NMR spectra of 3D printed BTCA-TAPB-COF monoliths (red) and powder BTCA-TAPB-COF (black). Asterisks indicate spinning side bands. b) PXRD diffractograms of 3D printed BTCA-TAPB-COF (red), powder BTCA-TAPB-COF (black), and calculated diffraction pattern (blue). c)  $\text{N}_2$  sorption isotherms at 77 K and d) pore size distribution calculated by NLDFT of 3D printed BTCA-TAPB-COF (red) and powder BTCA-TAPB-COF (black). e) SEM images of a 3D printed BTCA-TAPB-COF monolith at different magnifications.

hours or even days, in addition to other aggressive and costly treatments such as freeze drying or recrystallizations.<sup>[21,23]</sup> Upon solvent removal, the dry pieces experience a shrinking of  $\approx 65\%$  of their original volume but retain their shape without apparent cracks. This phenomenon has been previously observed in 3D printing with gels.<sup>[31,32]</sup>

#### 2.4. Characterization of the 3D Printed COFs

The composition, morphology, and structure of the 3D printed COF specimens were characterized by Fourier-transform infrared spectroscopy (FTIR), solid-state  $^{13}\text{C}$  cross-polarization magic angle spinning NMR ( $^{13}\text{C}$ -CP/MAS-NMR), SEM, and powder X-ray diffraction (PXRD).  $\text{N}_2$  sorption isotherms at 77 K as well as mercury intrusion porosimetry were obtained to characterize the porosity of the prints.

FTIR and  $^{13}\text{C}$ -CP/MAS-NMR confirmed the formation of BTCA-TAPB-COF. The FTIR spectrum (Figure S9, Supporting Information) exhibited the characteristic imine vibration at  $1623\text{ cm}^{-1}$ , while the rest closely resembles a typical BTCA-TAPB-COF powder. Similar to previous findings on BTCA-TAPB-COF nanoparticles, the FTIR revealed stronger residual aldehyde and amine bands than those obtained from powders with larger particle sizes. The bands at  $1698\text{ cm}^{-1}$  (C=O stretch) and  $3452, 3367,$  and  $3216\text{ cm}^{-1}$  (N-H stretches) exhibited enhanced intensities, which are attributed to the large number of unreacted groups at the edges of the nanoparticles.<sup>[28]</sup> However, no residual signals from CTAB or SDS could be observed, indicating the complete removal of the surfactants from the 3D printed structures.

The  $^{13}\text{C}$ -CP/MAS-NMR spectrum (Figure 2a) displayed a signal at  $157\text{ ppm}$ , corresponding to the imine carbon and the rest of

the aromatic signals characteristic of this material, and no signals from either of the surfactants.

PXRD measurements (Figure 2b) confirmed the formation of a crystalline structure with characteristic peaks at  $5.7^\circ, 10.0^\circ, 11.6^\circ,$  and  $25.5^\circ$ , corresponding respectively to the (100), (110), (200), and (001) crystal planes of BTCA-TAPB-COF. The broad signals in the diffraction pattern indicated the nanoparticle nature of the 3D printed COF, consistent with the broad peaks observed in the diffractogram of the powder COF nanoparticles as well as in previous reports.<sup>[28]</sup>

$\text{N}_2$  adsorption/desorption isotherms at 77 K showed a typical type I isotherm (Figure 2c) characteristic of microporous materials. The Brunauer–Emmett–Teller (BET) surface area, calculated using the BET surface identification (BETSI) algorithm,<sup>[33]</sup> was determined to be of  $735\text{ m}^2\text{ g}^{-1}$  (Figures S10 and S11, Supporting Information), which represents 47% of the theoretical maximum surface area of  $1563\text{ m}^2\text{ g}^{-1}$ , as calculated with the PoreBlazer software.<sup>[34]</sup> This compares very well to, and is even slightly higher than, the value obtained for the powder form of BTCA-TAPB-COF, which is  $676\text{ m}^2\text{ g}^{-1}$ , representing a 43% of the theoretical maximum surface area.<sup>[28]</sup> The total pore volume measured at  $P/P_0 = 0.95$  was  $0.96\text{ cm}^3\text{ g}^{-1}$ , and the pore size distribution (Figure 2d) obtained through non-local density functional theory (NLDFT) revealed a pore size of  $1.4\text{ nm}$ , consistent with the theoretical value. The pore size distribution also showed some mesoporosity, likely arising from the aggregated-nanoparticle nature of the 3D printed COF and its foam-like morphology. Furthermore, the linear increase in adsorption in the middle section of the isotherm reveals the presence of macroporosity in the samples.

In order to study and quantify this macroporosity mercury intrusion porosimetry was performed. It is important to note that our 3D printed COF monoliths are robust enough to endure

mercury impregnation without collapsing, which is very uncommon in the field and to the best of our knowledge, has only been recently reported in COF-rGO composites<sup>[35]</sup> or densified COF monoliths.<sup>[36]</sup> The 3D printed COFs present a continuous increase in mercury uptake with increased intrusion pressure (Figure S12, Supporting Information), which implies an increase in cumulative intrusion with decreasing pore diameter (Figure S13, Supporting Information). The resulting macropore size distribution has a maximum at 40–50  $\mu\text{m}$ , with a median pore diameter of 22  $\mu\text{m}$ . This broad distribution covers the whole macropore range from 200  $\mu\text{m}$  to 50 nm and extends into the mesopore range down to 25 nm. From the cumulative pore volume measured by this method a total pore volume of 18.3  $\text{cm}^3 \text{g}^{-1}$  and a macropore surface area of 85  $\text{m}^2 \text{g}^{-1}$  are obtained, while the porosity of the sample is calculated to be 92.3%. Therefore, the 3D printed COF monoliths displayed a diverse range of porosity, encompassing micro-, meso-, and macroporosity, covering all three types of pore size distribution within the material.

Bulk and apparent (skeletal) densities of 0.0504 and 0.6561  $\text{g cm}^{-3}$ , respectively, are obtained from the mercury porosimetry measurements. This bulk density agrees well with the geometric density calculated by dividing the mass of the sample by its volume, as measured with a digital caliper, which was found to be between 0.02 and 0.04  $\text{g cm}^{-3}$ . These values are exceptionally low and comparable to the densities previously reported for COF aerogels.<sup>[37–39]</sup>

The microscopic morphology of the COF prints was examined using SEM. At low magnification (Figure 2e-i), the 3D printed COFs presented a homogeneous, smooth surface with no apparent cracks, while the foam-like morphology was revealed at higher magnification (Figure 2e-ii). In the high magnification images (Figure 2e-iii), individual BTCA-TAPB-COF nanoparticles of  $\approx 20$  nm in diameter are observed, consistent with the nanoparticle size determined for the COF-based ink. These nanoparticles aggregated into nanofibers, giving rise to the foam-like morphology observed in the lower magnification images and contributing to the material's macroporosity, as observed in the mercury porosimetry.

To demonstrate the versatility of our 3D printing approach, we successfully printed and fully characterized another COF, namely TA-TAPB-COF (TA: terephthalaldehyde). The same protocol developed for BTCA-TAPB-COF was followed, with slight adjustments to the colloid's concentration and the printing parameters. The gelation of TA-TAPB-COF occurs faster, and therefore, operating under the same conditions optimized for BTCA-TAPB-COF resulted in failed prints and clogging of the printing head. The 3D printed TA-TAPB-COF was fully characterized by SEM, FTIR,  $^{13}\text{C}$ -CP/MAS-NMR, PXRD, and  $\text{N}_2$  sorption isotherms at 77 K. The experimental data obtained (Figures S14–S24, Supporting Information) were in agreement with those previously described for the conventional synthesis of TA-TAPB-COF.<sup>[40]</sup>

Interestingly, previous attempts to isolate this COF's nanoparticles as a powder resulted in an amorphous material after flocculation and activation. We hypothesize that this might be due to the bulk addition of alcohol to the colloid, which causes a sudden change of the solvent inside the COF pores that can disorganize the layers. This effect would be more pronounced in TA-

**Table 1.** Young's modulus, specific modulus, and density of our 3D printed COF monoliths and other COF aerogels reported in the literature.

Material	Young's modulus [kPa]	Specific modulus [ $\text{Pa m}^3 \text{kg}^{-1}$ ]	Density [ $\text{g cm}^{-3}$ ]
3D printed BTCA-TAPB-COF, parallel	56	1120	0.0504 <sup>a</sup>
3D printed BTCA-TAPB-COF, perpendicular	65	1290	0.0504 <sup>a</sup>
TAPB-BTCA-AGCOF [37]	4.07	209	0.0195
PPDA-BTCA-AGCOF [37]	1.77	85	0.0208
TAPB-PDA-AGCOF [37]	0.77	45	0.0173

<sup>a</sup> Density data measured by mercury porosimetry.

TAPB-COF than BTCA-TAPB-COF, as this material has a larger pore size and a smaller  $\pi$  surface, and thus weaker  $\pi$ - $\pi$  stacking interactions holding the crystalline structure. On the other hand, inside the microfluidic printing head this change of solvent occurs in a slow, diffusion-controlled manner that is less likely to disrupt the crystalline structure of the COF, allowing us to obtain the activated material with its crystalline structure intact.

Finally, and as a proof-of-concept study, the 3D printing of a series of other COFs are at different stages of optimization in our laboratory. These materials are based on different combinations of monomers (TFP: 1,3,5-triformylphloroglucinol; TAPT: 2,4,6-tris(4-aminophenyl)-1,3,5-triazine; HZ: hydrazine; TAPM: tetrakis(4-aminophenyl)methane) and include  $\beta$ -ketoamine-based COFs, such as TFP-TAPB-COF<sup>[41,42]</sup> and TFP-TAPT-COF<sup>[43,44]</sup>; and azine-based COFs, such as ACOF-1 (BTCA-HZ-COF)<sup>[45]</sup> and COF-JLU2 (TFP-HZ-COF)<sup>[46]</sup> (Figures S25–S29, Supporting Information).

## 2.5. Evaluation of the Mechanical Properties

Mechanical stability plays a crucial role in the long-term application of these structures, as mechanically unstable pieces could result in breakage and formation of powder, which would cause a loss of performance over time. In order to assess the mechanical properties of our 3D printed BTCA-TAPB-COF monoliths, we conducted uniaxial compression tests. Several cubic specimens (dimensions 8.7 mm  $\times$  8.7 mm  $\times$  8.7 mm) were printed and tested in both directions, parallel and perpendicular to the printing direction (Figure 3a,b). The stress-strain curves (Figure 3c) exhibit a linear elastic region, where compression is reversible, and a densification region, in which the stress increased rapidly with increasing strain, indicating irreversible compression. The stress-strain relationship in the elastic region follows Hook's law, with the stress increasing linearly with strain (Figures S30 and S31, Supporting Information). Young's moduli, calculated from this region, were found to be  $56 \pm 14$  kPa for the parallel direction and  $65 \pm 12$  kPa for the perpendicular direction, which are about one order of magnitude larger than those previously reported for the same BTCA-TAPB-COF in its aerogel form and other aerogels from different COFs (Table 1). Moreover, the specific moduli (Young's modulus over density) were calculated, and they are also about one order of magnitude larger than those previously reported.

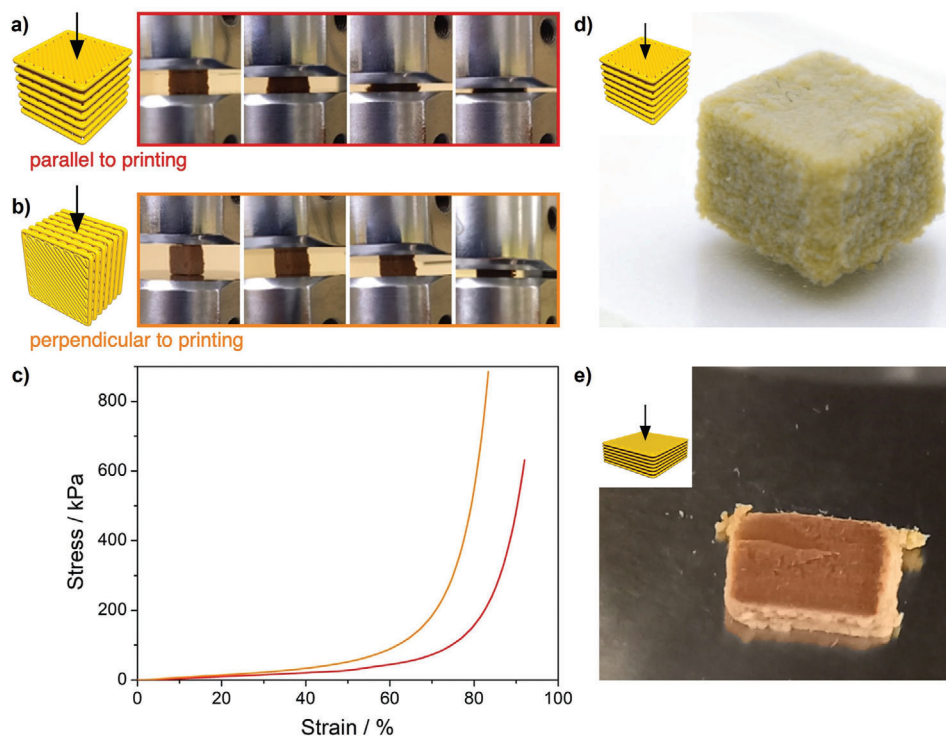


**Figure 3.** a,b) Schematic representation and photographs of the uniaxial compression tests for BTCA-TAPB-COF cubes parallel and perpendicular to the printing direction, respectively. c) Compression stress-strain curves obtained for the 3D printed BTCA-TAPB-COF cubes parallel (red) and perpendicular (orange) to the printing direction. d,e) Photographs of a BTCA-TAPB-COF cube before and after the compression test, respectively, with the cube having been pressed into a densified pellet.

After these compression tests the 3D printed cubes were analyzed by PXRD (Figure S32, Supporting Information), showing that they preserved their crystallinity after being compressed to 20%, 40%, or 60% strain, while they lost their crystallinity when compressed all the way to 90% strain and being pressed into densified pellets. Finally, we tested the behavior of the 3D printed COFs when subjected to multiple compression cycles to 10% strain. During these tests the samples increased their stiffness, especially from the first to the second cycle and from the second to the third cycle. After that, the behavior of the samples and the value of Young's modulus became increasingly more stable; after the 15th cycle, the changes were hardly noticeable. After these tests, the 3D printed cubes reduced their size by  $\approx 8\%$  of their original dimension along the compression axis, showing some degree of material fatigue.

These results indicate that 3D printing can significantly enhance the mechanical properties of COF aerogels by increasing their stiffness. This higher mechanical stability has already proven useful by making our 3D printed COF aerogels suitable for mercury porosimetry analysis, which commonly leads to structural collapse of these kind of soft aerogels.

Interestingly, in all of these experiments, some differences were observed between the samples measured in parallel and perpendicular directions. The Young's modulus was found to be  $\approx 15\%$  larger in the perpendicular direction than in the parallel direction (Table 1). Furthermore, the densification region started at a lower strain in the perpendicular direction compared to the

parallel one. The perpendicular sample reached the force limit of our load cell (50 N) before getting to a compression of 85%, whereas the parallel sample could be compressed to 90% strain at a lower stress. The samples were compressed into a densified pellet in both cases, as seen in Figure 3e.

The observed anisotropic behavior in the mechanical properties of the printed BTCA-TAPB-COF monoliths can be attributed to the directional alignment of the printed layers. In the parallel direction, where the layers were aligned perpendicular to the compression axis, lower stiffness, and a higher compression before densification were observed. Conversely, higher stiffness and faster densification at lower strains were observed in the perpendicular direction, where the printed layers were aligned parallel to the compression axis. This anisotropic behavior is consistent with previous findings from previous studies on other 3D printed materials, where the printing direction significantly impacts the mechanical properties.<sup>[47]</sup>

### 3. Conclusion

We have engineered a novel and versatile approach for the 3D printing of free-standing, binder-free, macroscopic COF architectures. Based on previously developed aqueous COF colloid, we have formulated a stable aqueous COF-based ink that can be successfully printed with a microfluidic-based printing head. Through this system, we achieved precise control over the ink's gelation process, enabling a layer-by-layer printing of pure COF monoliths with arbitrary shapes. Our approach utilizes water as a



solvent and operates at room temperature and atmospheric pressure, eliminating the need for toxic organic solvents.

Our strategy offers a solution to the long-standing challenge of processability for COFs and opens up new opportunities for their application in various fields. Importantly, our technology can be readily adapted to other COFs with slight adjustments and holds promise for the 3D printing of metal-organic frameworks (MOFs) as well. The ability to control the macroscopic size of COF structures is of utmost importance for their practical utilization, and our work represents a significant step toward achieving this goal. Our research has broad implications across multiple areas, including energy storage, catalysis, and sensing, and is expected to inspire further advancements in COF- and MOF-based additive manufacturing, for the realization of advanced materials with unprecedented properties and capabilities.

## 4. Experimental Section

Most chemicals and solvents were obtained from Aldrich Chemical Co. and used without further purification. TAPB was synthesized following a previously reported method<sup>[48]</sup> with slight modifications (see below). BTCA, terephthalaldehyde, CTAB, SDS, and PEG (20000 BioUltra) are commercially available and were used as received without further purification. FTIR spectra were recorded in a Perkin Elmer Spectrum 100 with a PIKE Technologies MIRAcle Single Reflection Horizontal ATR (attenuated total reflection) accessory with a spectral range of 4000–550 cm<sup>-1</sup>. Solution <sup>1</sup>H NMR and <sup>13</sup>C NMR spectra were recorded on a 300 MHz Bruker AVANCE spectrometer and are internally referenced to the residual solvent signals (CDCl<sub>3</sub>,  $\delta = 7.26$  ppm for <sup>1</sup>H NMR,  $\delta = 77.00$  ppm for <sup>13</sup>C NMR). <sup>1</sup>H NMR data were reported as chemical shift ( $\delta$  ppm), multiplicity (*s* = singlet, *d* = doublet, *bs* = broad singlet), coupling constant *J* (Hz), and integration. Solid-state <sup>13</sup>C-CP/MAS-NMR spectra were recorded on a Bruker AV 400 WB spectrometer using a 4 mm probe with zirconia rotors at a rotation frequency of 10 kHz. PXRD patterns were collected with a Panalytical X'Pert PRO diffractometer using Cu-K $\alpha$ 1 radiation ( $\lambda = 1.5406$  Å). Samples were mounted on a flat sample plate and measured with a step size of 0.03° and an exposure time of 1.5 s step<sup>-1</sup>. N<sub>2</sub> adsorption isotherms were measured using a Micromeritics ASAP2020 volumetric instrument under static adsorption conditions. Samples were previously activated at 120 °C overnight and outgassed to 10<sup>-6</sup> bar. BET surface areas were obtained using the BETSI algorithm.<sup>[33]</sup> Mercury porosimetry measurements were carried out on a Micromeritics AutoPore IV 9510 mercury intrusion-extrusion porosimeter with a resolution ranging from 4 nm to 360  $\mu$ m (3.6  $\times$  10<sup>5</sup> nm<sup>2</sup>). Samples were previously dried at 110 °C overnight and degassed for 15 min under vacuum before analysis, which was performed in the 0 to 60 000 psi range. Viscosity measurements were performed in an AND SV-10 vibrational viscosimeter at temperatures of 28 and 35 °C using a 10 mL sample container. DLS measurements were carried out using a Vasco 1 particle size analyzer from Cordouan Technologies. Measurements were carried out at 90° scattering angle at 35 °C, and the correlation function was collected until the signal-to-noise ratio was below 1% (typically 30–40 s). The viscosity of the solvent was corrected with the experimental viscosity of the sample. The hydrodynamic diameter was determined from the corner of the L-curve obtained with the SBL algorithm using the NanoQ analysis software. SEM images were acquired with a Hitachi S-800 microscope. Samples were previously coated with chromium in a Quorum Q150T-S sputter. The coating thickness was 7 nm for the nanoparticles drop-casted onto SiO<sub>2</sub> and 12 nm for the 3D printed monoliths. For critical point drying the solvent exchanged prints were placed in an open polypropylene box, sealed with a piece of dialysis tubing (Spectra/Por 1, MWCO: 6–8 kDa), and introduced into an SPI-DRY Critical Point Dryer – Jumbo. The chamber was filled with liquid CO<sub>2</sub> at 10 °C and 50 bar for half an hour. Then, the exchanged ethanol was removed through a purge valve, followed by flushing with fresh liquid CO<sub>2</sub>. This process was

repeated a total of seven times, and then the temperature was raised to 40 °C to reach the supercritical CO<sub>2</sub> state. Finally, the chamber was slowly vented at 8 bar h<sup>-1</sup> to atmospheric pressure. Uniaxial compression tests were carried out on an Instron 3400 Series Universal Testing Machine with a 50 N load cell. Samples were compressed to the desired maximum strain at a rate of 0.5 mm min<sup>-1</sup>, with a preload of 0.02 or 0.05 N.

**Synthesis of 1,3,5-tris-(4-nitrophenyl)benzene:** To a suspension of 4'-nitroacetophenone (15 g, 90.8 mmol) in absolute ethanol (90 mL) at 0 °C SiCl<sub>4</sub> (30 mL, 262 mmol) was added dropwise.<sup>[48]</sup> The solution turned clear during the addition, and then a yellow precipitate was formed. The reaction was refluxed overnight, cooled to room temperature, and saturated ammonium chloride (150 mL) was added. The mixture was stirred for 15 min, the solid was allowed to settle, and the supernatant was removed and replaced with water (250 mL). The washing procedure was repeated three times with water and then DMF (150 mL) was added, and the solid was collected by centrifugation (5 min, 4000 rpm). The supernatant was removed, solvent (150 mL) was added, and the mixture was centrifuged. This process was repeated five times with DMF, until the supernatant was clear, and three times with THF, affording an off-white solid that was dried under vacuum (5 g, 37%). This product is insoluble in any common deuterated solvent. FTIR (ATR)  $\tilde{\nu}$  (cm<sup>-1</sup>): 1594, 1510, 1349, 1055, 940, 862, 843, 814, 794, 748, 689.

**Synthesis of 1,3,5-tris-(4-aminophenyl)benzene (TAPB):** 1,3,5-Tris-(4-nitrophenyl)benzene (5.0 g, 11.3 mmol) and Pd/C (10% wt., 500 mg) were suspended in ethanol (130 mL), heated to reflux, and hydrazine hydrate (64%, 16.5 mL) was added dropwise through an addition funnel.<sup>[48]</sup> After refluxing for 4 h, another portion of hydrazine hydrate (64%, 16.5 mL) was added dropwise, and the mixture refluxed overnight. The reaction was hot filtered through a 1 cm Celite pad, the Celite was washed with hot THF (200 mL) to extract the precipitated product, and the solution was cooled to room temperature. The solvent was removed under reduced pressure, during which white crystals of TAPB were formed. The crystals were filtered, washed with cold water, and dried under vacuum to yield 3.63 g (91%) of the title compound. <sup>1</sup>H NMR (300 MHz, CDCl<sub>3</sub>)  $\delta$  (ppm): 7.60 (s, 3H, Benz), 7.51 (d, <sup>3</sup>J = 9 Hz, 6H, Ph), 6.78 (d, <sup>3</sup>J = 9 Hz, 6H, Ph), 3.74 (bs, 6H, -NH<sub>2</sub>). <sup>13</sup>C NMR (75 MHz, CDCl<sub>3</sub>)  $\delta$  (ppm): 145.8, 142.0, 131.9, 128.2, 122.9, 115.4.

**Synthesis of BTCA-TAPB-COF Colloids:** 1,3,5-benzenetricarbaldehyde (276 mg, 1.70 mmol) was dissolved in DMSO (1.50 mL) under sonication and with gentle heating. The resulting solution was added dropwise under sonication to a mixture of an aqueous solution of CTAB (120 mL, 0.1 M) and an aqueous solution of SDS (3.70 mL, 0.1 M). The resulting suspension was sonicated and heated gently until a clear, colorless solution was achieved. Separately, 1,3,5-tris-(4-aminophenyl)benzene (600 mg, 1.70 mmol) was dissolved in DMSO (0.90 mL) under sonication. This solution was added dropwise to a mixture of an aqueous solution of CTAB (120 mL, 0.1 M), an aqueous solution of SDS (3.70 mL, 0.1 M), and glacial acetic acid (12.0 mL), yielding a clear, colorless solution. Finally, the two aqueous solutions were mixed, and the mixture immediately turned orange. The solution was deoxygenated by performing 3 vacuum-argon cycles and allowed to react at 30 °C for 72 h. A completely transparent red colloidal solution was obtained.

**Isolation of BTCA-TAPB-COF Powder:** Ethanol (20 mL) was added to the BTCA-TAPB-COF colloid (20 mL), resulting in the precipitation of a yellow solid. The mixture was centrifuged (5 min 4000 rpm), the supernatant was removed, and the solid was resuspended in fresh EtOH (20 mL). The mixture was stirred for 30 min, and the washing procedure was repeated a total of eight times. The final solid was suspended in the minimal amount of EtOH and subjected to supercritical CO<sub>2</sub> activation, yielding 55.4 mg (92%) of BTCA-TAPB-COF nanoparticles as a pale yellow powder.

**Preparation of BTCA-TAPB-COF Ink:** The BTCA-TAPB-COF colloid (20 mL) was placed inside a piece of dialysis membrane (Spectra/Por1, MWCO = 6–8 kDa), sealed, and submerged in an aqueous solution of PEG 20000 (30 mL, 100 mg mL<sup>-1</sup>). The system was kept at 30 °C for 24 h, resulting in a reduction of the colloid's volume of  $\approx$ 45% to a final volume of 11 mL of COF-based ink. This ink was kept at 30 °C until its use for 3D printing, being stable for at least 6 months.

**Resin Printing of the Microfluidic Reactor:** The microfluidic reactor was printed in a commercial Elegoo Saturn LCD 3D printer using Anycubic 3D printing UV sensitive resin. The layer height was set at 0.05 mm with an exposure time of 5 s and a lifting distance of 5 mm. The bottom ten layers had an exposure time of 50 s to ensure adhesion to the printing plate. After printing, the reactor was washed with 2-propanol to remove leftover uncured resin, ensuring the reactor's internal channels were clean. Finally, the reactor was cured for 120 s under a dual 385–405 nm UV curing lamp.

**3D Printing Parameters for BTCA-TAPB-COF:** The digital 3D models were created with the Tinkercad CAD software with the desired shapes and exported as STL files. These files were loaded into the Ultimaker Cura 4.11 slicing software to generate the g-code files with the following parameters: the line width was set at 0.5 mm, the height of the first three layers at 0.22 mm, the height of all the other layers at 0.27 mm and the printing speed at 6 mm s<sup>-1</sup>. The wall line count was three, the wall line width 0.5 mm, and the infill 100% with the zig-zag pattern. The rest of the parameters were left unchanged from the “Standard Quality – 0.2 mm” preloaded profile. The models were placed 1 cm away from the origin on both axis (x-y) to make sure that the material coming out of the printer while the flows are stabilizing does not interfere with the print. The g-code files were then loaded into the 3D printer with a microSD card, and the BTCA-TAPB-COF ink and 2-butanol were fed into the system with a pressure-based microfluidic flow controller (MFCS-EZ from Fluigent), each passing through a flow rate sensor (L flow units from Fluigent). The pressures were 240 mbar (corresponding to 110 μL min<sup>-1</sup>) for the BTCA-TAPB-COF ink and 35 mbar (corresponding to 90 μL min<sup>-1</sup>) for 2-butanol. Once the flow of both streams was stable the tip of the microfluidic reactor was placed ≈0.5 mm above the printing substrate and the printing program started. A typical print lasted ≈40–60 min. When the printing was finished, the 2-butanol was slowly removed and replaced with ethanol to wash the printed monoliths. The solvent was exchanged with fresh ethanol six times over 3 days, and the pieces were finally activated via supercritical CO<sub>2</sub> drying.

**Synthesis of TA-TAPB-COF Colloids:** Terephthalaldehyde (135 mg, 1.00 mmol) was dissolved in DMSO (0.375) under sonication. The resulting solution was added dropwise under sonication to a mixture of an aqueous solution of CTAB (32.5 mL, 0.1 M) and an aqueous solution of SDS (3.60 mL, 0.1 M). The resulting suspension was sonicated and heated gently until achieving a clear, colorless solution. Separately, 1,3,5-tris(4-aminophenyl)benzene (235 mg, 0.669 mmol) was dissolved in DMSO (0.375 mL) under sonication. This solution was added dropwise to a mixture of an aqueous solution of CTAB (60.5 mL, 0.1 M), an aqueous solution of SDS (6.70 mL, 0.1 M), and glacial acetic acid (20.0 mL), yielding a clear, colorless solution. Finally, the two aqueous solutions were mixed and the mixture turned bright yellow. The solution was deoxygenated by performing 3 vacuum-argon cycles and allowed to react at 30 °C for 72 h. A completely transparent yellow colloidal solution was obtained.

**Isolation of TA-TAPB-COF Powder:** Ethanol (20 mL) was added to the TA-TAPB-COF colloid (20 mL), resulting in the precipitation of a yellow solid. The mixture was centrifuged (5 min 4000 rpm), the supernatant was removed, and the solid was resuspended in fresh EtOH (20 mL). The mixture was stirred for 30 min, and the washing procedure was repeated eight times. The final solid was suspended in the minimal amount of EtOH and subjected to supercritical CO<sub>2</sub> activation, yielding 52.5 mg (88%) of TA-TAPB-COF nanoparticles as a bright yellow powder.

**Preparation of TA-TAPB-COF Ink:** The TA-TAPB-COF colloid (20 mL) was placed inside a piece of dialysis membrane (Spectra/Por1, MWCO = 6–8 kDa), sealed, and submerged in an aqueous solution of PEG 20000 (30 mL, 100 mg mL<sup>-1</sup>). The system was kept at 30 °C for 24 h, reducing the colloid's volume by ≈45% to a final volume of 11 mL of COF-based ink. This ink was kept at 30 °C until its use for 3D printing, being stable for at least 6 months.

**3D Printing Parameters for TA-TAPB-COF:** The digital 3D models were created with the Tinkercad CAD software with the desired shapes and exported as STL files. These files were loaded into the Ultimaker Cura 4.11 slicing software to generate the g-code files with the following parameters: the line width was set at 0.5 mm, the height of the first three layers at 0.22 mm, the height of all the other layers at 0.27 mm and the printing

speed at 6 mm s<sup>-1</sup>. The wall line count was 3, the wall line width 0.5 mm, and the infill 100% with the zig-zag pattern. The rest of the parameters were left unchanged from the “Standard Quality – 0.2 mm” preloaded profile. The models were placed 1 cm away from the origin on both axis (x-y) to make sure that the material coming out of the printer while the flows were stabilizing did not interfere with the print. The g-code files were then loaded into the 3D printer with a microSD card and the TA-TAPB-COF ink and 2-butanol were fed into the system with a pressure-based microfluidic flow controller (MFCS-EZ from Fluigent), each passing through a flow rate sensor (L flow units from Fluigent). The pressures 16 mbar (35 μL min<sup>-1</sup>) for the TA-TAPB-COF ink and 240 mbar (740 μL min<sup>-1</sup>) for 2-butanol. Once the flow of both streams was stable, the tip of the microfluidic reactor was placed ≈0.5 mm above the printing substrate, and the printing program started. A typical print lasted ≈40–60 min. When the printing was finished, the 2-butanol was slowly removed and replaced with ethanol to wash the printed monoliths. The solvent was exchanged with fresh ethanol six times over 3 days, and the pieces were finally activated via supercritical CO<sub>2</sub> drying.

## Supporting Information

Supporting Information is available from the Wiley Online Library or from the author.

## Acknowledgements

This work had been supported by the Spanish MINECO (PID2019-106268GB-C32, PID2022-138908NB-C31, TED2021-129886B-C42, PDC2022-133498-I00, and PID2020-116612RB-C33). The authors acknowledge the service from the MiNa Laboratory at IMN and funding from CM (project S2018/NMT-4291 TEC2SPACE), MINECO (project CSIC13-4E-1794) and EU (FEDER, FSE). F.Z. acknowledges financial support from the Spanish Ministry of Science and Innovation, through the “María de Maeztu” Programme for Units of Excellence in R&D (CEX2018-000805-M). S.P., J.P.-L., and F. Z. also acknowledge support from the European Innovation Council under grant Agreement 101047081 (EVA). The authors acknowledge the support from the “(MAD2D-CM)-UAM” project funded by Comunidad de Madrid, by the Recovery, Transformation and Resilience Plan, and by NextGenerationEU from the European Union.

## Conflict of Interest

The authors declare no conflict of interest.

## Data Availability Statement

The data that support the findings of this study are available in the supplementary material of this article.

## Keywords

3D printing, covalent organic frameworks, inks, processing

Received: November 22, 2023  
Published online: December 21, 2023

- [1] A. P. Côté, A. I. Benin, N. W. Ockwig, M. O'keeffe, A. J. Matzger, O. M. Yaghi, *Science* **2005**, 310, 1166.

- [2] F. Haase, B. V. Lotsch, *Chem. Soc. Rev.* **2020**, *49*, 8469.
- [3] R. Liu, K. T. Tan, Y. Gong, Y. Chen, Z. Li, S. Xie, T. He, Z. Lu, H. Yang, D. Jiang, *Chem. Soc. Rev.* **2021**, *50*, 120.
- [4] Z. Wang, S. Zhang, Y. Chen, Z. Zhang, S. Ma, *Chem. Soc. Rev.* **2020**, *49*, 708.
- [5] J. Guo, D. Jiang, *ACS Cent. Sci.* **2020**, *6*, 869.
- [6] Z. Xia, Y. Zhao, S. B. Darling, *Adv. Mater. Interfaces* **2021**, *8*, 2001507.
- [7] R. Freund, O. Zaremba, G. Arnauts, R. Ameloot, G. Skorupskii, M. Dinca, A. Bavykina, J. Gascon, A. Ejsmont, J. Goscianska, M. Kalmutzki, U. Lächelt, E. Ploetz, C. S. Diercks, S. Wuttke, *Angew. Chem., Int. Ed.* **2021**, *60*, 23975.
- [8] K. Geng, T. He, R. Liu, S. Dalapati, K. T. Tan, Z. Li, S. Tao, Y. Gong, Q. Jiang, D. Jiang, *Chem. Rev.* **2020**, *120*, 8814.
- [9] D. Rodríguez-San-Miguel, F. Zamora, *Chem. Soc. Rev.* **2019**, *48*, 4375.
- [10] J. Á. Martín-Illán, J. A. Suárez, J. Gómez-Herrero, P. Ares, D. Gallego-Fuente, Y. Cheng, D. Zhao, D. Maspoch, F. Zamora, *Adv. Sci.* **2022**, *9*, 2104643.
- [11] D. A. Vazquez-Molina, G. S. Mohammad-Pour, C. Lee, M. W. Logan, X. Duan, J. K. Harper, F. J. Uribe-Romo, *J. Am. Chem. Soc.* **2016**, *138*, 9767.
- [12] J.-Y. Lee, J. An, C. K. Chua, *Appl. Mater. Today* **2017**, *7*, 120.
- [13] T. D. Ngo, A. Kashani, G. Imbalzano, K. T. Q. Nguyen, D. Hui, *Composites, Part B* **2018**, *143*, 172.
- [14] L. J. Tan, W. Zhu, K. Zhou, *Adv. Funct. Mater.* **2020**, *30*, 2003062.
- [15] N. Haghdadi, M. Laleh, M. Moyle, S. Primig, *J. Mater. Sci.* **2021**, *56*, 64.
- [16] H. Thakkar, S. Eastman, Q. Al-Naddaf, A. A. Rownaghi, F. Rezaei, *ACS Appl. Mater. Interfaces* **2017**, *9*, 35908.
- [17] G. J. H. Lim, Y. Wu, B. B. Shah, J. J. Koh, C. K. Liu, D. Zhao, A. K. Cheetham, J. Wang, J. Ding, *ACS Mater. Lett.* **2019**, *1*, 147.
- [18] S. Sultan, H. N. Abdelhamid, X. Zou, A. P. Mathew, *Adv. Funct. Mater.* **2019**, *29*, 1805372.
- [19] J. Dhainaut, M. Bonneau, R. Ueoka, K. Kanamori, S. Furukawa, *ACS Appl. Mater. Interfaces* **2020**, *12*, 10983.
- [20] S. Lawson, A.-A. Alwakwak, A. A. Rownaghi, F. Rezaei, *ACS Appl. Mater. Interfaces* **2020**, *12*, 56108.
- [21] M. Zhang, L. Li, Q. Lin, M. Tang, Y. Wu, C. Ke, *J. Am. Chem. Soc.* **2019**, *141*, 5154.
- [22] X. Liu, G. J. H. Lim, Y. Wang, L. Zhang, D. Mullangi, Y. Wu, D. Zhao, J. Ding, A. K. Cheetham, J. Wang, *Chem. Eng. J.* **2021**, *403*, 126333.
- [23] A. K. Mohammed, S. Usgaonkar, F. Kanheerampockil, S. Karak, A. Halder, M. Tharkar, M. Addicoat, T. G. Ajithkumar, R. Banerjee, *J. Am. Chem. Soc.* **2020**, *142*, 8252.
- [24] M. Martínez-Fernández, R. Gavara, S. Royuela, L. Fernández-Ecija, J. I. Martínez, F. Zamora, J. L. Segura, *J. Mater. Chem. A* **2022**, *10*, 4634.
- [25] M. Zhang, H. Mei, P. Chang, L. Cheng, *J. Mater. Chem. A* **2020**, *8*, 10670.
- [26] Z. Lyu, G. J. H. Lim, J. J. Koh, Y. Li, Y. Ma, J. Ding, J. Wang, Z. Hu, J. Wang, W. Chen, Y. Chen, *Joule* **2021**, *5*, 89.
- [27] C.-K. Su, J.-Y. Lin, *Anal. Chem.* **2020**, *92*, 9640.
- [28] C. Franco, D. Rodríguez-San-Miguel, A. Sorrenti, S. Sevim, R. Pons, A. E. Platero-Prats, M. Pavlovic, I. Szilágyi, M. L. Ruiz Gonzalez, J. M. González-Calbet, D. Bochicchio, L. Pesce, G. M. Pavan, I. Imaz, M. Cano-Sarabia, D. Maspoch, S. Pané, A. J. De Mello, F. Zamora, J. Puigmartí-Luis, *J. Am. Chem. Soc.* **2020**, *142*, 3540.
- [29] M. D. Hager, P. Greil, C. Leyens, S. Van Der Zwaag, U. S. Schubert, *Adv. Mater.* **2010**, *22*, 5424.
- [30] D. L. Taylor, M. In Het Panhuis, *Adv. Mater.* **2016**, *28*, 9060.
- [31] D. Oran, S. G. Rodrigues, R. Gao, S. Asano, M. A. Skylar-Scott, F. Chen, P. W. Tillberg, A. H. Marblestone, E. S. Boyden, *Science* **2018**, *362*, 1281.
- [32] M. A. Saccone, R. A. Gallivan, K. Narita, D. W. Yee, J. R. Greer, *Nature* **2022**, *612*, 685.
- [33] D. Fairen-Jimenez, J. W. M. Osterrieth, J. Rampersad, D. Madden, N. Rampal, L. Skoric, B. Connolly, M. D. Allendorf, V. Stavila, J. L. Snider, R. Ameloot, J. Marreiros, C. Ania, D. Azevedo, E. Vilarrasa-Garcia, B. F. Santos, X.-H. Bu, Z. Chang, H. Bunzen, N. R. Champness, S. L. Griffin, B. Chen, R.-B. Lin, B. Coasne, S. Cohen, J. C. Moreton, Y. J. Colón, L. Chen, R. Clowes, F.-X. Coudert, et al., *Adv. Mater.* **2022**, *34*, 2201502.
- [34] L. Sarkisov, R. Bueno-Perez, M. Sutharson, D. Fairen-Jimenez, *Chem. Mater.* **2020**, *32*, 9849.
- [35] C. Li, S. Cao, J. Lutzki, J. Yang, T. Konegger, F. Kleitz, A. Thomas, *J. Am. Chem. Soc.* **2022**, *144*, 3083.
- [36] M. E. Carrington, N. Rampal, D. G. Madden, D. O'nolan, N. P. M. Casati, G. Divitini, J. Á. Martín-Illán, M. Tricarico, R. Cepitis, C. Çamur, T. Curtin, J. Silvestre-Albero, J.-C. Tan, F. Zamora, S. Taraskin, K. W. Chapman, D. Fairen-Jimenez, *Chem* **2022**, *8*, 2961.
- [37] J. Á. Martín-Illán, D. Rodríguez-San-Miguel, O. Castillo, G. Beobide, J. Perez-Carvajal, I. Imaz, D. Maspoch, F. Zamora, *Angew. Chem., Int. Ed.* **2021**, *60*, 13969.
- [38] D. Zhu, Y. Zhu, Q. Yan, M. Barnes, F. Liu, P. Yu, C.-P. Tseng, N. Tjahjono, P.-C. Huang, M. M. Rahman, E. Egap, P. M. Ajayan, R. Verduzco, *Chem. Mater.* **2021**, *33*, 4216.
- [39] X. Li, Z. Jia, J. Zhang, Y. Zou, B. Jiang, Y. Zhang, K. Shu, N. Liu, Y. Li, L. Ma, *Chem. Mater.* **2022**, *34*, 11062.
- [40] B. J. Smith, A. C. Overholts, N. Hwang, W. R. Dichtel, *Chem. Commun.* **2016**, *52*, 3690.
- [41] C. Li, H. Li, C. Li, X. Ren, Q. Yang, *Chin. J. Catal.* **2021**, *42*, 1821.
- [42] D. Kaleeswaran, P. Vishnoi, R. Murugavel, *J. Mater. Chem. C* **2015**, *3*, 7159.
- [43] H. Li, J. Liu, M. Wang, X. Ren, C. Li, Y. Ren, Q. Yang, *Sol. RRL* **2021**, *5*, 2000641.
- [44] R. Gomes, A. Bhaumik, *RSC Adv.* **2016**, *6*, 28047.
- [45] Z. Li, X. Feng, Y. Zou, Y. Zhang, H. Xia, X. Liu, Y. Mu, *Chem. Commun.* **2014**, *50*, 13825.
- [46] Z. Li, Y. Zhi, X. Feng, X. Ding, Y. Zou, X. Liu, Y. Mu, *Chem. - Eur. J.* **2015**, *21*, 12079.
- [47] J. Chen, X. Liu, Y. Tian, W. Zhu, C. Yan, Y. Shi, L. B. Kong, H. J. Qi, K. Zhou, *Adv. Mater.* **2022**, *34*, 2102877.
- [48] C. Bao, R. Lu, M. Jin, P. Xue, C. Tan, T. Xu, G. Liu, Y. Zhao, *Chem. - Eur. J.* **2006**, *12*, 3287.